

# Electron Energy-Loss Safe-Dose Limits for Manganese Valence Measurements in Environmentally Relevant Manganese Oxides

Kenneth J. T. Livi,<sup>\*,†</sup> Brandon Lafferty,<sup>‡,§</sup> Mengqiang Zhu,<sup>‡,#</sup> Shouliang Zhang,<sup>||</sup> Anne-Claire Gaillot,<sup>⊥</sup> and Donald L. Sparks<sup>‡</sup>

<sup>†</sup>The High-Resolution Analytical Electron Microbeam Facility of the Integrated Imaging Center Departments of Earth and Planetary Sciences and Biology, Johns Hopkins University, Baltimore, Maryland 21218, United States

<sup>‡</sup>Plant and Soil Sciences, University of Delaware, Newark, Delaware 19717-1303, United States

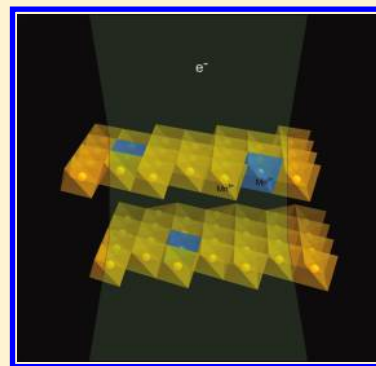
<sup>§</sup>U.S. Army Engineer Research & Development Center, 3909 Halls Ferry Road, Vicksburg, Mississippi 39180, United States

<sup>||</sup>Texas Material Institute, University of Texas, Austin, Texas 78712, United States

<sup>⊥</sup>Institut des Matériaux Jean Rouxel (IMN), Université de Nantes, CNRS, 2 rue de la Houssinière, BP 32229, 44322 Nantes Cedex 3, France

## Supporting Information

**ABSTRACT:** Manganese (Mn) oxides are among the strongest mineral oxidants in the environment and impose significant influence on mobility and bioavailability of redox-active substances, such as arsenic, chromium, and pharmaceutical products, through oxidation processes. Oxidizing potentials of Mn oxides are determined by Mn valence states (2+, 3+, 4+). In this study, the effects of beam damage during electron energy-loss spectroscopy (EELS) in the transmission electron microscope have been investigated to determine the “safe dose” of electrons. Time series analyses determined the safe dose fluence (electrons/nm<sup>2</sup>) for todorokite (10<sup>6</sup> e/nm<sup>2</sup>), acid birnessite (10<sup>5</sup>), triclinic birnessite (10<sup>4</sup>), randomly stacked birnessite (10<sup>3</sup>), and δ-MnO<sub>2</sub> (<10<sup>3</sup>) at 200 kV. The results show that meaningful estimates of the mean Mn valence can be acquired by EELS if proper care is taken.



## INTRODUCTION

Mn exists in the 2+, 3+, and 4+ valence states in natural environment and, most of the time, as Mn<sup>4+</sup>-oxide minerals (here referred to as MnO<sub>x</sub>) with more or less structural Mn<sup>2+</sup> and Mn<sup>3+</sup> impurities. MnO<sub>x</sub> are found in complex mixtures of phases in various degrees of crystalline perfection and with fine-grained size in a wide variety of oceanic and terrestrial environments, such as soils, ocean floors, fresh-water sediments, and deserts. An important fraction of MnO<sub>x</sub> under oxic conditions is believed to form from oxidation of Mn<sup>2+</sup> by O<sub>2</sub> via microbially mediated processes.

Although MnO<sub>x</sub> minerals in the environment are generally far less abundant than other minerals, such as iron-oxides, the importance of MnO<sub>x</sub> in controlling environmental chemical processes is not in accordance with their abundance.<sup>1</sup> MnO<sub>x</sub> minerals tend to contain a large amount of structural defects, such as vacant sites in birnessite, and are negatively charged under most pH conditions.<sup>2,3</sup> The role of MnO<sub>x</sub> is evident from studies on metal adsorption<sup>4</sup> and on redox-active organic and inorganic species controlling their toxicity, mobility and bioavailability.<sup>5–8</sup> These characteristics make MnO<sub>x</sub> one of the most important solid components of the aquatic and terrestrial ecosystems.

In order to understand MnO<sub>x</sub> redox behaviors during oxidation of Mn<sup>2+</sup> to MnO<sub>x</sub> in their formation or during

MnO<sub>x</sub> reduction to lower valences by reducing substances, it is critical to quantify Mn mean valence. Since MnO<sub>x</sub> samples collected from the environment are often admixtures with other mineral phases, it is desirable to obtain mean valence information with spatial resolution. We define mean valence as

$$V_{\text{bar}} = 2a_{\text{Mn}^{2+}} + 3b_{\text{Mn}^{3+}} + 4c_{\text{Mn}^{4+}} \quad (1)$$

where *a*, *b*, and *c* are atomic fractions of the three valence states.

There are four ways of obtaining *V*<sub>bar</sub>: classic chemical titration, X-ray absorption spectroscopy, and related techniques, such as scanning transmission X-ray microscopy, X-ray photoelectron spectroscopy, and electron energy-loss spectroscopy (EELS) in the transmission electron microscope (TEM). EELS has the best spatial resolution of all techniques and can achieve relative errors as low as 2%.<sup>9</sup> Given these characteristics, EELS is the method of choice for examining the valence state of fine-grained Mn phases. However, the analytical protocols must be carefully determined to ensure that systematic errors and artifacts are minimized. This is the goal of this paper. We have chosen the most relevant MnO<sub>x</sub> forms

Received: October 4, 2011

Revised: December 2, 2011

Accepted: December 13, 2011

Published: December 13, 2011

found in nature and those synthetic forms commonly used in laboratory experiments: todorokite (Tod), acid birnessite (AcidBir), triclinic birnessite (TrBir), randomly stacked birnessite (RSB, a disordered form of triclinic birnessite), and  $\delta$ -MnO<sub>2</sub>.

EELS in a transmission electron microscope has been widely used to determine the oxidation state and bonding environment of metals.<sup>10–15</sup> The majority of previous studies have focused on engineered materials and only a few studied environmentally relevant species, such as MnO<sub>x</sub> minerals.<sup>16–18</sup> The examination of MnO<sub>x</sub> minerals is particularly complicated because these minerals contain Mn cation defects and –OH groups because of the defects, metal impurities, and water in their structure, and tend to damage by electron beam faster than simple metal oxides. They have the potential for Mn to be either oxidized by the loss of hydrogen or reduced by loss of oxygen. This was pointed out in the literature when measuring Mn and Fe mean valence states.<sup>19–21</sup> To date, there has not been a systematic study of electron beam damage rates for MnO<sub>x</sub>.

## METHODS

**Preparation of MnO<sub>x</sub>.** Several MnO<sub>x</sub> minerals were used in this research. Pyrolusite was purchased from Sigma-Aldrich. Todorokite used in this research was originally collected from Cuba (Monte Negro Mine, Oriente Province) and was kindly provided by Dr. Jeffrey E. Post at the Smithsonian National Museum of Natural History.

Randomly stacked birnessite and TrBir syntheses followed the method described by Yang and Wang.<sup>22</sup> The procedure utilizes pure O<sub>2</sub> gas to oxidize a Mn(OH)<sub>2</sub> suspension in an ice water bath. Half of the suspension was centrifuged and the solid, that is, RSB, was washed with deionized (DI) water and freeze-dried. The rest of the suspension was aged at 60 °C for 48 h in an oven. The aging process increased the MnO<sub>6</sub> layer stacking order of the RSB and resulted in TrBir, a more crystalline form.<sup>23</sup>

Acid birnessite synthesis followed the method of McKenzie<sup>24</sup> and Feng et al.<sup>25</sup> A 65.4 mL of concentrated HCl was pumped at 1 mL min<sup>-1</sup> to a 1 L of 0.4 M boiling KMnO<sub>4</sub> solution by a peristaltic pump. The suspension was stirred vigorously during the HCl addition. Because of the evaporation of HCl during the addition, KMnO<sub>4</sub> was not completely consumed, as indicated by the purple color of the suspension. The solid was collected by centrifuge, washed with DI water and then freeze-dried.  $\delta$ -MnO<sub>2</sub> was synthesized using the redox reaction between KMnO<sub>4</sub> and Mn(NO<sub>3</sub>)<sub>2</sub>. The specific procedure can be found in ref 26.

**Chemical Titration.** The average Mn  $V_{\text{bar}}$  of the samples was determined by the oxalate titration method. Briefly, a small mass (50–100 mg) of each MnO<sub>x</sub> was added to 30 mL of a standardized 0.025 M Na<sub>2</sub>C<sub>2</sub>O<sub>4</sub> solution and 5 mL of 5.4 M H<sub>2</sub>SO<sub>4</sub>. The suspension was heated and stirred until the solid was completely dissolved. The solution was then cooled and diluted to 50 mL with deionized water. A 20-mL aliquot of solution was then heated and titrated with a standardized 0.02 M KMnO<sub>4</sub> solution until a faint pink color resulting from excess MnO<sub>4</sub><sup>-</sup> was detected by eye in solution. The remainder of the diluted sample solution was retained for total aqueous Mn quantification by inductively coupled plasma atomic emission spectrometry (ICP-AES). Mn  $V_{\text{bar}}$  in each mineral was determined by averaging at least three replicates.

**Electron Energy-Loss Spectroscopy.** Electron energy-loss spectroscopy was performed on a Philips CM 300 field emission gun (FEG) operating at 197 kV for all samples, and additionally, at 97 kV for  $\delta$ -MnO<sub>2</sub>. The extraction voltage of the microscope was operated at low values (3.2 kV at the higher accelerating potential and 2.5 kV at the lower accelerating potential) to ensure the best energy resolution which was nominally 0.8 eV. The spectra were collected in diffraction mode (image-coupled) using a Gatan GIF 200 with a 2 mm entrance aperture, 0.2 eV dispersion, 4 mrad semiangle of convergence, and a 15 mrad collection angle. This setup ensures the validity of dipole selection rules for the electronic transitions from the 2p core level.

Samples were prepared by dropping suspensions in water or ethanol on Ti metal-coated carbon film grids. The position of the Ti L<sub>2</sub> absorption peak position was used as an internal energy calibration.<sup>16</sup>

To minimize the electron-beam-induced effects, which will cause chemical reduction of Mn<sup>4+</sup> in the samples, we varied the electron exposure. The degree of electron exposure (fluence) was varied by changing beam current using both the gun lens and first condenser lens (spot size) and the flux by setting various beam diameters with the second condenser lens (C2). Since changing the convergence of the beam with C2 lens affects the focus of the zero-loss peak (ZLP) at the spectrometer slit, care was taken to set a beam diameter and then focus the ZLP.

The fluence was calculated knowing the beam current as measured from a calibration of the exposure time on the main viewing screen, the beam diameter, and exposure time.<sup>20</sup> With very beam sensitive materials, damage may begin instantaneously—even when a low intensity beam illuminates the sample. Therefore, the initial exposure time during analysis setup could only be estimated. To estimate this time, another observer timed the analyst and determined the average setup duration. This was then added to the fluence for all samples, regardless of beam damage rates.

The L<sub>2,3</sub> edges of Mn from mixed-valence minerals can be modeled by a multiple linear least-squares (MLLS) fitting of the three valence end-member spectra. This method was applied successfully to Fe L<sub>2,3</sub> edges by fitting experimental reference spectra to unknown Fe-silicates.<sup>9,13</sup> Zhang et al.<sup>16</sup> determined that the MLLS fitting of reference standards was the best method for determining  $V_{\text{bar}}$  as opposed to calibration curves using L<sub>2,3</sub> peak heights or positions. This method was employed here with the addition of time-series analyses to assess beam damage. Pyrolusite (MnO<sub>2</sub>) and manganite (MnOOH) were used as Mn<sup>4+</sup> and Mn<sup>3+</sup> standards, respectively, and were previously studied by Zhang et al.<sup>16</sup> Synthetic manganosite (MnO) was used for the Mn<sup>2+</sup> standard when beam damage caused mean valences to be less than 3. The three standards did not exhibit beam damage or valence changes over the course of ten analyses 10 s each. Mathematically, the Mn L<sub>2,3</sub> spectra from unknown samples can be represented according to eqs 2 and 3

$$\frac{I(\Delta E)}{\int_{\Delta E=635\text{eV}}^{\Delta E=660\text{eV}} I(\Delta E)d(\Delta E)} = a \times \frac{I_1(\Delta E)}{\int_{\Delta E=635\text{eV}}^{\Delta E=660\text{eV}} I_1(\Delta E)d(\Delta E)} + b \times \frac{I_2(\Delta E)}{\int_{\Delta E=635\text{eV}}^{\Delta E=660\text{eV}} I_2(\Delta E)d(\Delta E)} \quad (2)$$

$$\frac{I(\Delta E)}{\int_{\Delta E=635\text{eV}}^{\Delta E=660\text{eV}} I(\Delta E)d(\Delta E)} = b \times \frac{I_1(\Delta E)}{\int_{\Delta E=635\text{eV}}^{\Delta E=660\text{eV}} I_1(\Delta E)d(\Delta E)} + c \times \frac{I_2(\Delta E)}{\int_{\Delta E=635\text{eV}}^{\Delta E=660\text{eV}} I_2(\Delta E)d(\Delta E)} \quad (3)$$

where  $a$ ,  $b$ , and  $c$  are the fractions of  $\text{Mn}^{4+}$ ,  $\text{Mn}^{3+}$ , and  $\text{Mn}^{2+}$ , respectively, in the mixed valence samples, and  $I$  is the integrated intensity over an energy-loss region defined by  $\Delta E$ . The addition of a  $\text{Mn}^{2+}$  reference is necessary for analysis of extremely damaged samples. Although an equation can be formulated to include all three valence references, the resulting best-fit  $V_{\text{bar}}$  was not significantly different from results of a two reference fit. For EEL spectrometers with better resolution, small amounts of  $\text{Mn}^{2+}$  in  $\text{Mn}^{3+} + \text{Mn}^{4+}$  dominated phases may be detected. Given a resolution of 0.8 eV, only two reference fits were deemed sufficient.

Both the reference spectra and mixed-valence spectra were processed in a consistent way. The background intensity at the Mn  $L_{2,3}$  edge was subtracted by fitting an inverse power-law function for a range of 40–50 eV before the edge onset and extrapolating this function to higher energies. Following the background subtraction, the multiple scattering contribution in the high-loss region was removed by deconvolution with the low-loss region,<sup>27</sup> including the zero-loss peak, which was acquired consecutively from the same specimen region as that used for the core-loss spectrum, but at a much lower fluence rate to prevent CCD saturation. The continuum contribution resulting from transition from 2p states to the continuum band was removed following the two-step functions.<sup>9</sup>

Since the goal of this study is to determine the electron “safe dose” of various  $\text{MnO}_x$  minerals, analytical time series were collected. Most of the minerals studied here show some valence changes with time. From these data, the value of  $V_{\text{bar}}$  can be calculated in four ways: (1) a numerical average of all model values yielding the statistical standard deviation of the population and an error of the mean (all errors are reported as 95% confidence), (2) a regression back to time zero giving a slope and intercept with associated errors, (3) a summation of all undamaged spectra and a goodness of fit Pearson's correlation coefficient, and (4) an average of summed spectra from several different areas of the sample. Method 1 works best when there is no obvious damage during the data collection. The error simply measures the variation due to counting statistics and the fitting method. Method 2 yields interpretable errors and is useful for samples that experience beam damage. A complication with this method stems from the choice of when

damage begins. Inclusion of data from damaged material often will bias the intercept toward more oxidized  $V_{\text{bar}}$  values. Method 3 allows for a precise fitting of the peak shape but does not allow for a simple estimate of the analytical error for one fitting. With method 4, several areas were collected for each sample and the average of sum spectra and the standard error can be calculated. In theory, all four methods should yield the same value, but in practice, there are some differences. We report all four estimates.

## RESULTS

**Images and Electron Diffraction.** A collection of the images and diffraction patterns for each sample is presented in the Supporting Information Figure S1. Todorokite contains relatively large crystals ( $6.5 \mu\text{m} \times 100 \text{nm}$ ) that have many defects related to the distribution of tunnels within each crystal. Acid birnessite ( $100 \times 10 \text{nm}$ ) and RSB ( $1000 \times 50 \text{nm}$ ) have similar shapes and form rosettes of equant sheets. Triclinic birnessite is intermediate in size and forms laths  $500 \times 200 \times 10 \text{nm}$ .  $\delta\text{-MnO}_2$  contains both crystalline sheets and amorphous material and has the finest grain size ( $20 \times 5 \text{nm}$ ).

Electron diffraction patterns of each of the samples are unique. The SAED pattern of Tod contains strong diffraction intensity indicative of large crystals but also contains radial streaks that arise from the linear defects related to the disordering of tunnel positions within the crystals. Therefore, many of the low index reflections are wiped out. Triclinic birnessite, AcidBir, and  $\delta\text{-MnO}_2$  have similar SAED patterns with TrBir showing the highest degree of crystalline order of the three, and  $\delta\text{-MnO}_2$  the lowest, by virtue of peak sharpness. Randomly stacked birnessite SAED has sharp peaks but has split rings most likely due to the presence of different stacking sequences.

**EELS Analyses. Todorokite.** A typical EELS spectrum of Tod is presented in Figure 1 (inset). This spectrum was a sum

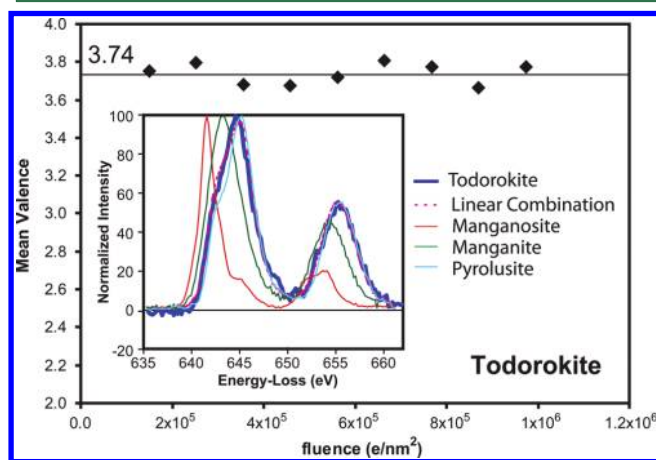


**Figure 1.** Analytical time series and an EELS sum spectrum along with reference and MLLS fitted spectra for Tod.

of nine 10 s analyses. The spectra for the three valence references and a linear combination of  $\text{Mn}^{3+}$  and  $\text{Mn}^{4+}$  are also given. There is a good fit between the experimental and modeled spectra, which in this case yields a calculated  $V_{\text{bar}}$  of 3.74 (see also Table 1). Typical correlation coefficients for fitting of individual spectra were around 0.987.

A time series obtained to determine whether there is a change in the valence state as fluence increased is also given in

Table 1. Chemical Titration and EELS Comparison

estimation method	EELS												
	chemical titration		fit of sum of n damage-free spectra from one area			ave of n individual damage-free spectra from one area			intercept from damage-free spectra		ave of summed damage-free spectra from m areas		
	$V_{\text{bar}}$	$2\sigma$	$V_{\text{bar}}$	cor. coeff	n	$V_{\text{bar}}$	$2\sigma$	n	$V_{\text{bar}}$	$2\sigma$	$V_{\text{bar}}$	$2\sigma$	m
randomly-stacked birnessite	3.60	0.03	3.66	0.983	14	3.69	0.08	10	3.71	0.09	3.61	0.04	6
triclinic birnessite	3.71	0.04	3.74	0.984	10	3.72	0.05	10	3.72	0.07	3.71	0.05	11
todorokite	3.76	0.04	3.74	0.996	9	3.74	0.04	9	3.74	0.04	3.76	0.06	7
acid birnessite	3.89	0.03	3.87	0.991	10	3.86	0.06	10	3.87	0.05	3.89	0.03	10
$\delta$ -MnO <sub>2</sub>	3.96	0.05	nc <sup>a</sup>			nc			4.04 <sup>b</sup>	0.11	nc		

<sup>a</sup>nc = not calculated. <sup>b</sup>Average of 10 intercepts at 97 kV.

Figure 1. The plot indicates that the  $V_{\text{bar}}$  does not change even after a total fluence of  $2.5 \times 10^5 \text{ e/nm}^2$ . The numerical average of all the  $V_{\text{bar}}$  data within this time series is  $3.74 \pm 0.04$ , while the intercept is also  $3.74 \pm 0.04$ . Although it is possible to evaluate each time series for changes in valence with fluence, it is less time-consuming to sum the ten spectra collected during the determined “safe dose” period for Tod, and then fit references to the sum spectra. Fitting of the summed spectra yields an average  $V_{\text{bar}} = 3.76 \pm 0.06$  with an average fitting correlation coefficient of 0.996.

**Triclinic Birnessite.** Figure 2a contains a sum spectrum of ten 5 s analyses of TrBir and includes a time series analysis. The

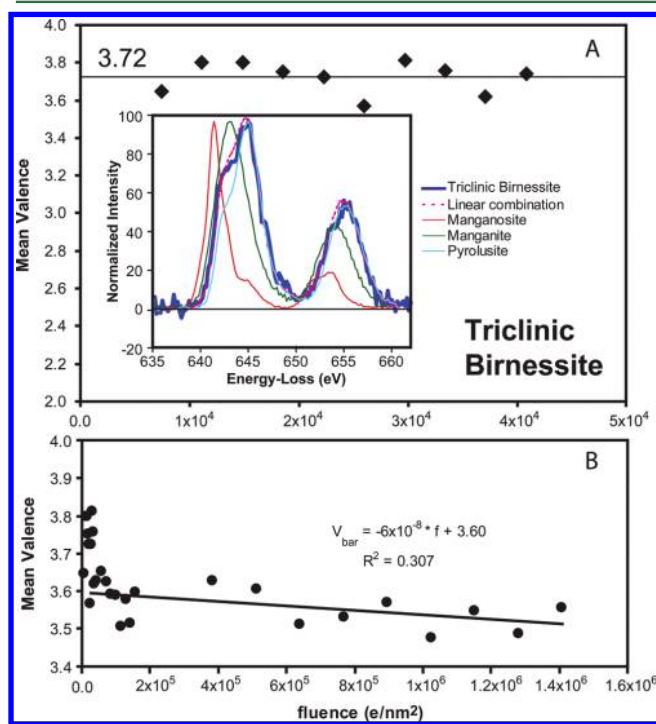


Figure 2. (A) EELS sum and MLLS fitted spectra, and analytical time series of TrBir. (B) Extended time series of TrBir showing a damage plateau.

increased noise in the spectrum, as compared to Tod, is a result of a decreased initial fluence ( $7.2 \times 10^3 \text{ e/nm}^2$  at 5 s). Fitting of individual spectra of TrBir gave correlation coefficients of around 0.965. Triclinic birnessite remains damage free up to fluences of  $10^4 \text{ e/nm}^2$ . Fitting of the summed spectra yields a  $V_{\text{bar}} = 3.74$  with a correlation coefficient of 0.984, while the numerical average of ten individual spectra results in a  $V_{\text{bar}} =$

$3.72 \pm 0.05$ . Linear fitting of the same data results in an intercept of  $3.72 \pm 0.07$ . Fitting of eleven different sum spectrum with fluences less than  $1.0 \times 10^5 \text{ e/nm}^2$  results in  $V_{\text{bar}} = 3.71 \pm 0.05$ .

When the fluence is increased further,  $V_{\text{bar}}$  drops to a lower plateau with a numerical average  $3.56 \pm 0.03$  and an intercept  $V_{\text{bar}} = 3.60 \pm 0.02$  (Figure 2b). This indicates that if the initial fluence is too high, there might not be any analyses unaffected by damage, and the damage plateau could be erroneously interpreted as a valid  $V_{\text{bar}}$  measurement.

**Randomly-Stacked Birnessite.** A sum spectrum of ten 5 s spectrum of RSB is shown in Figure 3 at an initial fluence of  $3.6$

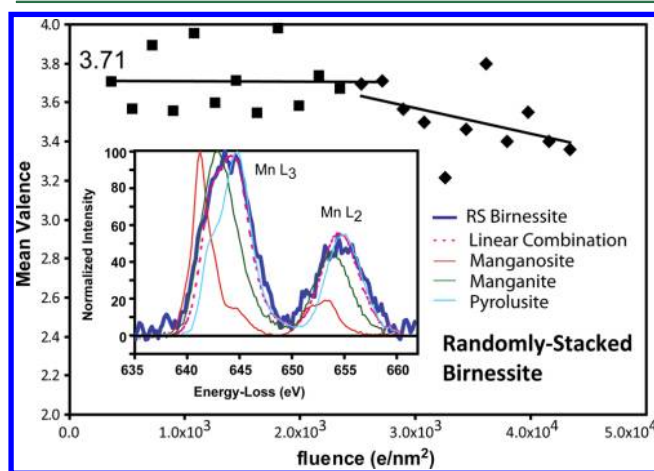
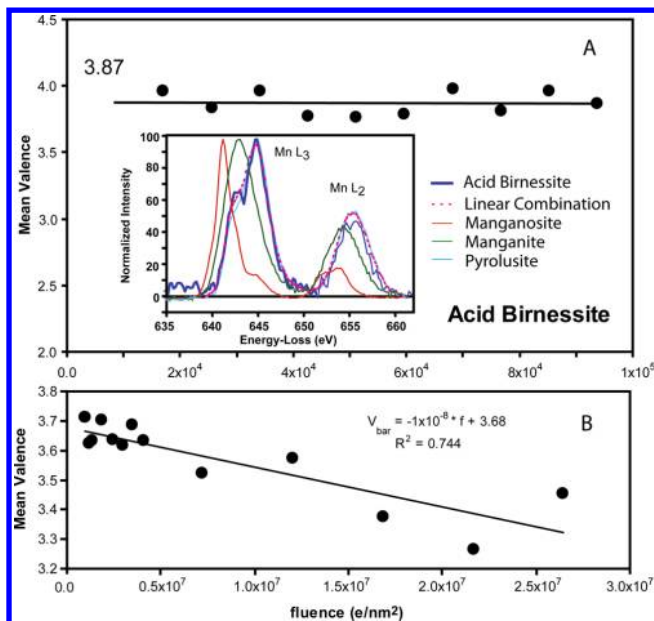


Figure 3. EELS sum and MLLS fitted spectra, and analytical time series of RSB.

$\times 10^3 \text{ e/nm}^2$ . Fitting of individual spectra of RSB gave correlation coefficients of around 0.901. The time series in Figure 3 indicates that RSB remains damage free only until a fluence of  $3 \times 10^4 \text{ e/nm}^2$ . Fitting of the summed spectra in Figure 3 yields a  $V_{\text{bar}} = 3.66$  with a correlation coefficient of 0.983, while the numerical average of these data results in a  $V_{\text{bar}} = 3.69 \pm 0.08$ . Linear fitting of the same data results in an intercept of  $3.71 \pm 0.09$ . Although this area resulted in a  $V_{\text{bar}}$  that was relatively high, the average of summed spectra from six different areas was  $3.61 \pm 0.04$ . This is evidence of valence heterogeneity within this sample. After a fluence of  $3 \times 10^4 \text{ e/nm}^2$ , RSB shows a decrease in the oxidation state of Mn. Linear extrapolation of the damaged spectra yields an intercept of  $3.96 \pm 0.30$ .

**Acid Birnessite.** Acid birnessite data are presented in Figure 4a. A sum spectrum from ten 5 s spectra was fitted and resulted in a  $V_{\text{bar}} = 3.87$  with a correlation coefficient of 0.991. The



**Figure 4.** (A) EELS sum and MLLS fitted spectra, and analytical time series of AcidBir. (B) Extended time series of AcidBir.

numerical average of these ten fitted spectra was  $3.86 \pm 0.06$ . A linear regression of the time series data gave an intercept value of  $3.87 \pm 0.05$ . AcidBir remains undamaged up to fluences of  $1 \times 10^5 \text{ e/nm}^2$ . An extended time series (Figure 4b) indicates that AcidBir damages after  $1 \times 10^5 \text{ e/nm}^2$  resulting in an extrapolated intercept of  $3.68 \pm 0.05$ . The average of ten undamaged sum spectra was  $3.89 \pm 0.03$ .

$\delta\text{-MnO}_2$ . Spectra of  $\delta\text{-MnO}_2$  have been acquired at low fluences ( $1.8 \times 10^3 \text{ e/nm}^2$ , 5 s), and therefore are very noisy (Figure 5a). Fitting of individual spectra of  $\delta\text{-MnO}_2$  gave correlation coefficients of around 0.88. Figure 5b graphically

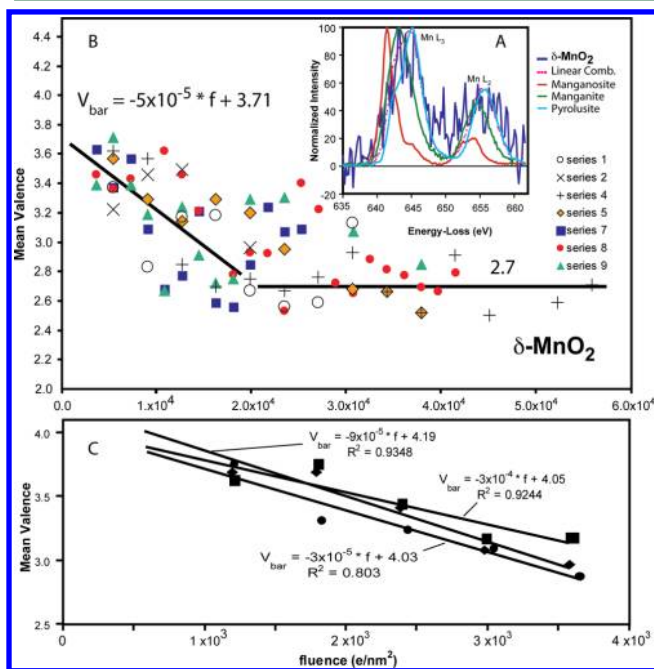


**Figure 5.** (A) A single spectrum of  $\delta\text{-MnO}_2$ . (B) Time series for  $\delta\text{-MnO}_2$  at 197 kV. (C) Time series for  $\delta\text{-MnO}_2$  at 97 kV and low fluence.

illustrates the rapid damage rate of  $\delta\text{-MnO}_2$ . Under the conditions of this experiment, there are no damage-free analyses of  $\delta\text{-MnO}_2$ . Several sets of data are presented in this plot. A linear extrapolation of all the data with fluences less than  $2 \times 10^4 \text{ e/nm}^2$  yields an intercept of  $3.71 \pm 0.13$ . After a fluence of  $\sim 2 \times 10^4 \text{ e/nm}^2$ ,  $V_{\text{bar}}$  ceases to reduce and plateaus at  $\sim 2.7$ .

Spectra of  $\delta\text{-MnO}_2$  were also collected at 97 kV to determine if the reduced energy of the beam has an effect on the rate of valence changes. Figure 5c demonstrates that even at the low fluence rate of  $5 \times 10^2 \text{ e/(nm}^2 \text{ s)}$  at 97 kV,  $\delta\text{-MnO}_2$  still damages rapidly. However, unlike the time series of previous samples, extrapolation of time series to time = 0 can yield meaningful values of  $V_{\text{bar}}$ . It follows that an accurate estimate of time = 0 is heavily dependent upon careful determinations of the beam setting time before acquisition begins. The average of 10 time series intercepts is  $4.04 \pm 0.11$ .

**Comparison to Chemical Titration Measurements.** A comparison of chemical titration and EELS average  $V_{\text{bar}}$  measurements is given in Table 1. There is extremely good agreement between results of chemical titration and the values from averaged summed spectra for all samples excluding  $\delta\text{-MnO}_2$  (although all values are within error). There is no difference in  $V_{\text{bar}}$  or errors, except for  $\delta\text{-MnO}_2$ , between titration and EELS. However, titration requires sample volumes of  $\sim 5 \mu\text{L}$  ( $10^{-6}$ ) while EELS needs only  $\sim 5$  attoliters ( $10^{-18}$ ), twelve orders of magnitude less.  $\delta\text{-MnO}_2$  has a much larger error in the EELS measurement than all the other samples; however, it is still possible to conclude that  $\delta\text{-MnO}_2$  is mainly  $\text{Mn}^{4+}$  within error.

DISCUSSION

Table 1 demonstrates that reliable determination of  $\text{Mn}^{3+}$  and  $\text{Mn}^{4+}$  can be obtained by EELS in most cases. The time series included here also demonstrate that caution must be exercised to assess whether beam damage is altering the measured valence state. Table 2 lists the estimated “safe fluence” for each of the studied samples.

**Table 2. EELS Maximum Fluences at 197 kV**

sample	max fluence (e/nm <sup>2</sup> )
todorokite	$> 1 \times 10^6$
acid birnessite	$1 \times 10^5$
triclinic birnessite	$5 \times 10^4$
randomly-stacked birnessite	$2.5 \times 10^3$
$\delta\text{-MnO}_2$	$< 1 \times 10^3$

The crystallinity of each sample was qualitatively assessed by TEM observation of grain sizes and amount of amorphous material present. There are clear differences in crystal sizes between the samples. However, we have not quantified their defect concentrations. Todorokite represents the sample with the largest crystal size, while  $\delta\text{-MnO}_2$  has the poorest crystallinity. Correspondingly, there are greater than two orders of difference in safe fluence between these two structures. The correlation between crystal size and safe fluence for the rest of the samples is not straightforward. In fact, for AcidBir, TrBir, and RSB, the safe fluence decreases with increasing grain size of the sheets (Table 2 and Supporting Information Figure S1). Two other factors may have a greater influence on the damage rate of  $\text{MnO}_x$  phases: defect concentration and coherent

scattering domain size. Since it has been our experience that electron damage can nucleate on defect sites, internal domain boundaries and crystal edges (which itself can be considered a “defect”), it is logical that a decrease in coherent scattering domain size and an increase in internal defects would cause an increase in beam damage susceptibility. In addition, the rate of damage does not correlate with  $V_{\text{bar}}$ . This indicates that damage rate is not a function of the redox potential of  $\text{MnO}_x$  materials. Corroborating this is the fact that pyrolusite does not readily damage even though it is nearly pure  $\text{Mn}^{4+}$ .

The worst case of beam damage comes from  $\delta\text{-MnO}_2$  that can be at times completely amorphous.  $\delta\text{-MnO}_2$  is problematic in that no safe dose has been measured for 197 kV. Lowering the beam energies to 97 kV did not significantly reduce damage even though less energy is imparted to the sample. It is likely that there was some reduction in the damage rate, but the low fluences yield noisy spectra and do not define a clear safe fluence of electrons. Therefore, the differences between 197 and 97 kV experiments cannot be determined. Additional evidence that 97 kV is “gentler” on  $\delta\text{-MnO}_2$  comes from observations that SAED patterns change within seconds to a pattern similar to manganosite ( $\text{MnO}$ ) at 197 kV, while damage proceeds more slowly (within tens of seconds at similar fluences) at 97 kV. More research would be necessary to determine the damage threshold at even lower kV. It is apparent from the time series analyses that one cannot rely simply on extrapolations to time zero. It is desirable to have some undamaged analyses in order to distinguish that portion of the curve from altered valence analyses, and finally, from analyses in the damage plateau. In addition, the damage rates reported here may differ for natural samples of birnessite and, in fact, even from other syntheses of the same material.

Toner et al.<sup>28</sup> demonstrated that it is possible to determine  $V_{\text{bar}}$  using scanning transmission X-ray microscopy (STXM) methods. In comparing their results to ours, three main points may be made. (1) STXM induces less damage in environmental samples than EELS, although it is not a damage-free technique. (2) STXM failed to distinguish variations of  $V_{\text{bar}}$  between 3.5 and 4. Most birnessite-type minerals have  $V_{\text{bar}}$  in this range, and this is where EELS becomes the method of choice, despite its tendency toward beam damage. (3) The precision of EELS is much better than STXM analyses, at present, and is comparable to chemical titration.

The ability to perform individual analyses on complexly intergrown nanoparticles is extremely powerful. With EELS analyses, the heterogeneity of natural samples can be assessed while also determining the extent of local chemical exchange. Core-to-rim variation can also be measured. In systems with slow reaction rates, rim compositions may reflect greater reaction progress than the bulk, and therefore, only analyses obtained at the nanoscale on rims have meaningful values. This study has shown for the first time that, given the proper care, quality representative Mn  $V_{\text{bar}}$  measurements can be made for natural birnessite-type samples. This opens up the possibility for more detailed studies of fine-grained natural samples and heterogeneous experimental products.

## ■ ASSOCIATED CONTENT

### ● Supporting Information

Figure S1 TEM images and selected area electron diffraction patterns. This material is available free of charge via the Internet at <http://pubs.acs.org>.

## ■ AUTHOR INFORMATION

### Corresponding Author

\*Phone: 410-516-8342. Fax: 410-516-7933. E-mail: [klivi@jhu.edu](mailto:klivi@jhu.edu).

### Present Address

#Earth Sciences Division, Lawrence Berkeley National Laboratory, Berkeley, CA 94720.

## ■ ACKNOWLEDGMENTS

This publication was made possible by the National Science Foundation EPSCoR Grant No. EPS-0814251, NSF EAR Grant No. 0544246 and the State of Delaware.

## ■ REFERENCES

- (1) Post, J. E. Manganese oxide minerals: Crystal structures and economic and environmental significance. *Proc. Natl. Acad. Sci. U. S. A.* **1999**, *96*, 3447–3454.
- (2) Makenzie, R. The adsorption of lead and other heavy metals on oxides of manganese and iron. *Aust. J. Soil Res.* **1980**, *18*, 61–73.
- (3) Manceau, A.; Lanson, B.; Drits, V. A. Structure of heavy metal sorbed birnessite. Part III: Results from powder and polarized extended X-ray absorption fine structure spectroscopy. *Geochim. Cosmochim. Acta* **2002**, *66*, 2639–2663.
- (4) Zhu, M.; Ginder-Vogel, M.; Sparks, D. L. Ni(II) sorption on biogenic Mn-oxides with varying Mn octahedral layer structure. *Environ. Sci. Technol.* **2010**, *44*, 4472.
- (5) Manceau, A.; Drits, V. A.; Silvester, E.; Bartoli, C.; Lanson, B. Structural mechanism of  $\text{Co}^{2+}$  oxidation by the phyllo-manganate busserite. *Am. Mineral.* **1997**, *82*, 1150–1175.
- (6) Murray, J. W.; Dillard, J. G. Oxidation of cobalt(II) adsorbed on manganese-dioxide. *Geochim. Cosmochim. Acta* **1979**, *43* (5), 781–787.
- (7) Oscarson, D. W.; Huang, P. M.; Defosse, C.; Herbillon, A. Oxidative power of Mn(IV) and Fe(III) oxides with respect to As(III) in terrestrial and aquatic environments. *Nature* **1981**, *291* (5810), 50–51.
- (8) Fredrickson, J. K.; Zachara, J. M.; Kennedy, D. W.; Liu, C.; Duff, M. C.; Hunter, D. B.; Dohnalkova, A. Influence of Mn oxides on the reduction of uranium(VI) by the metal-reducing bacterium *Shewanella putrefaciens*. *Geochim. Cosmochim. Acta* **2002**, *66*, 3247–3262.
- (9) van Aken, P. A.; Liebscher, B. Quantification of ferrous/ferri ratios in minerals: new evaluation schemes of Fe  $L_{2,3}$  electron energy-loss near-edge spectra. *Phys. Chem. Min.* **2002**, *29*, 188–200.
- (10) Garvie, L. A. J.; Craven, A. J. High-resolution parallel electron energy-loss spectroscopy of Mn  $L_{2,3}$ -edges in inorganic manganese compounds. *Phys. Chem. Min.* **1994**, *21*, 191–206.
- (11) Colella, M.; Lumpkin, G. R.; Zhangs, Z.; Buck, E. C.; Smith, K. L. Determination of uranium valence state in the brannerite structure using EELS, XPS, and EDX. *Phys. Chem. Min.* **2005**, *32*, 52–64.
- (12) van Aken, P. A.; Liebscher, B.; Styrsa, V. J. Quantitative determination of iron oxidation states in minerals using Fe  $L_{2,3}$ -edge energy-loss near-edge structure spectroscopy. *Phys. Chem. Min.* **1998**, *25*, 323–327.
- (13) Calvert, C. C.; Brown, A.; Brydson, R. Determination of the local chemistry of iron in inorganic and organic materials. *J. Electron Spec. Relat. Phenom.* **2005**, *143*, 173–187.
- (14) Schmid, H. K.; Mader, W. Oxidation states of Mn and Fe in various compound oxide systems. *Micron* **2006**, *37*, 426–432.
- (15) Daulton, T. L.; Little, B. J. Determination of chromium valence over the range Cr(0)–Cr(VI) by electron energy loss spectroscopy. *Ultramicrosc.* **2006**, *106*, 561–573.
- (16) Zhang, S.; Livi, K. J. T.; Gaillot, A.-C.; Veblen, D. R. Determination of manganese valence states in ( $\text{Mn}^{3+}$ ,  $\text{Mn}^{4+}$ ) minerals by electron energy-loss spectroscopy. *Am. Mineral.* **2010**, *95*, 1741–1746.
- (17) Garvie, L. A. J.; Burt, D. M.; Buseck, P. R. Nanometer-scale complexity, growth, and diagenesis in desert varnish. *Geology* **2008**, *36*, 215–218.

- (18) Calvert, C. C.; Gutzmer, J.; Banks, D. A.; Rainforth, W. M. EELS characterization and valence determination of Mn minerals from the Kalahara Manganese Field in South Africa. *J. Phys.: Conf. Ser.* **2008**, *126*, 012045.
- (19) Garvie, L. A. J.; Craven, A. J. Electron-beam-induced reduction of Mn<sup>4+</sup> in manganese oxides as revealed by parallel EELS. *Ultramicroscopy* **1994**, *54*, 83–92.
- (20) Garvie, L. A. J.; Zega, T. J.; Rez, P.; Buseck, P. R. Nanometer-scale measurements of Fe<sup>3+</sup>/ΣFe by electron energy-loss spectroscopy: A cautionary note. *Am. Mineral.* **2004**, *89*, 1610–1616.
- (21) Pan, Y.; Brown, A.; Brydson, R. Electron beam damage studies on 6-line ferrihydrite. *J. Phys.: Conf. Ser.* **2006**, *26*, 46–49.
- (22) Yang, D. S.; Wang, M. K. Syntheses and characterization of well-crystallized birnessite. *Chem. Mater.* **2001**, *13*, 2589–2594.
- (23) Yang, D. S.; Wang, M. K. Syntheses and characterization of birnessite by oxidizing pyrochroite in alkaline conditions. *Clays Clay Miner.* **2002**, *50* (1), 63–69.
- (24) McKenzie, R. M. The synthesis of birnessite, cryptomelane, and some other oxides and hydroxides of Manganese. *Miner. Magn.* **1971**, *38*, 493–502.
- (25) Feng, X.; Zhai, L.; Tan, W.; Liu, F.; He, J. Adsorption and redox reactions of heavy metals on synthesized Mn oxide minerals. *Environ. Pollution* **2007**, *147*, 366–373.
- (26) Lafferty, B.; Ginder-Vogel, M.; Sparks, D. L. Arsenite oxidation by a poorly crystalline manganese-oxide 1. Stirred-flow experiments. *Environ. Sci. Technol.* **2010**, *44*, 8460–8466.
- (27) Egerton, R. *Electron Energy-Loss Spectroscopy in the Electron Microscope*, 2nd ed.; Plenum/Springer: New York, 1996.
- (28) Toner, B.; Fakra, S.; Villalobos, M.; Warwick, T.; Sposito, G. Spatially resolved characterization of biogenic manganese oxide production within bacterial biofilm. *Appl. Environ. Microbiol.* **2005**, *71* (3), 1300–1310.